Signal-to-noise ratio improvements using anti-scatter grids with different object thicknesses and tube voltages

博 士 論 文

Signal-to-noise ratio improvements using anti-scatter grids with different object thicknesses and tube voltages

ディジタルX線画像における散乱線除去グリッドによる信号対雑音比改善効果の検討

氏　　名	國友　博史
主任指導教員	市川　勝弘　教　授
副指導教員	宮地　利明　教　授
提出年月日	2020年7月7日

Contents

Abstract

Purpose: The anti-scatter grid is a useful tool for improving image quality of general radiography to reduce influence of the scatter radiation. However, the appropriate object thickness to start using anti-scatter grids (grids) has not sufficiently investigated in previous studies, and thus we rigorously investigated the effectiveness of two generally used grids with grid ratios of 6 and 10 (G6 and G10) for different 50–200 mm thicknesses at tube voltages of 60–100 kV.

Methods: Acrylic phantoms with 30 × 30 cm^2 and different thicknesses were used to measure the signal-to-noise ratio improvement factors (SIFs) of grids. To evaluate the infants' conditions, field sizes of 225, 400, and 625 cm^2 were also evaluated at 60–80 kV. In addition, the signal difference-to-noise ratio (SDNR) was used to evaluate tube voltage dependencies of grids for each thickness.

Results: SIF values exceeded 1.0 for ≥70 mm thicknesses and mostly exceeded 1.07 for the 100 mm thickness with 400 cm^2 field size corresponding to a 1-year-old infant abdomen. The estimated dose reduction capabilities for a 1-year-old infant were approximately 15% using G10 at 70 and 80 kV. The tube voltage dependencies for grid use was almost not prominent for all conditions tested, except for some conditions that

are not clinically realistic.

Conclusions: G6 and G10 can improve SNR for ≥100mm thickness. The results from this work demonstrate approximately 15% dose reduction or image quality improvements at the same dose level for the use of G6 and G10 grids for 100mm thickness, traditionally excluded from the recommended grid use conditions.

List of Tables

List of Figures

List of Abbreviations

AL	aluminium
CsI	Caesium Iodide
DR	Digital Radiography
ESAK	Entrance Surface Air Kerma
FOM	Figure of Merit
FPD	Flat Panel Detector
G-	No Grid
NEQ	Noise Equivalent Quanta
G6	Grid Ratios of 6
G10	Grid Ratios of 10
mAs	Milliampere Seconds
PMMA	Poly(Methyl Methacrylate)
ROI	Region of Interest
SD	Standard Deviation
SDNR	Signal Difference to Noise Ratio
SF	Scatter Fraction

SIF Signal-to-noise Ratio Improvement Factor

SNR Signal-to-noise Ratio

Acknowledgments

There are many people I wish to thank for their kind support and mentorship during my Ph.D. studies. First and foremost, I would like to thank my supervisor Dr. Katsuhiro Ichikawa, for his encouragement and guidance. I have learned from him not only how to do research but also how to be a research scientist.

I would also like to thank my other Ichikawa laboratory members for their helpful comments throughout this project.

This work would not have been possible without the help and support from the scientists working on radiology at Nagoya city university hospital.

I am also thankful to Dr.Toshiaki Miyachi and Ph.D. Hiroki Kawashima at Kanazawa University whose seminal work has provided a basis for my thesis and whose discussions have been particularly helpful when there was no solution in sight.

Chapter 1

Introduction

In general radiography, a beam of x-rays is produced by a combination of x-ray generator and x-ray tube is projected toward the object. When a patient is irradiated with the x-rays, incident x-rays are attenuated by removing x-ray photons due to absorption and scattering caused by different interactions with the tissue. In the digital radiography (DR) formed with attenuated x-rays, the diagnostic performance is known to be decreased by the scatter radiation that significantly reduces object contrast. Thus, to improve the contrast degradation by the scatter radiation, anti-scatter grids (hereinafter, referred to as the “grid”) are generally used.

The scatter fraction (SF) has been known to increase with subject’s thickness and irradiated field size. Thus, in a clinical examination, the necessity of grid is determined predominantly by the subject’s thickness; generally, it is not used for extremities such as the hand and knee and pediatrics with small body sizes. According to several guidelines including pediatric-related ones and a review article, the grid should not be used for body parts with ≤100–120 mm thicknesses **[1-4]**. Results from previous studies were used as

references for the statements in the guidelines and review.

Dick et al. and Kalender et al. reported various scatter fraction data for different subject thicknesses, and the results were referred as one of the statements that subject contrast is markedly degraded when the body part is at least 100–120 mm **[5, 6]**. This condition is directly relevant to screen-film systems in which the image contrast cannot be manipulated without changing the film gamma. Conversely, since the DR system changes the image contrast characteristics by data manipulation in its image processing stage (e.g., use of look-up table), the signal-to-noise ratio (SNR) becomes an effective index for assessing the image quality; thus, the SNR improvement factor (SIF) has been used to evaluate grid performances. Chen et al. investigated SIFs for 50 and 170 mm thicknesses at 70 kV; grids tested were not effective for the 50 mm thickness **[7]**. Fetterly et al. provided SIF (K SNR in the paper) results for 100 to 500 mm thicknesses at 104 kV; SIF was improved by grids even from the 100 mm thickness **[8]**. SIF results for 200 mm thickness at 50, 70, and 100 kV were reported by Sandborg et al, showing that all types of grids used improved the SIF, while the SIF value varied depending on the cover and inter-space materials **[9]**. Thus, to our knowledge, detailed threshold thicknesses where the grid becomes recommendable for different tube voltages are yet unclear. If these are demonstrated through quantitative measurements, the information would

contribute to proper grid selection for infants and subjects with low thicknesses. Moreover, the effect of tube voltage on image quality under a grid use, which cannot be evaluated by SIF, has not been sufficiently evaluated to date.

This study aimed to measure SIFs for 50, 70, 100, 150, and 200 mm thicknesses with generally used grids, at 60, 70, 80, 90, and 100 kV, and to verify the threshold thickness to select the use of grids. In addition, the signal difference-to-noise ratio (SDNR), an image quality measure for DR system in the presence of a contrast object, was measured to assess tube voltage dependencies of the image quality with the grid for each thickness.

Chapter 2

Materials and methods

2.1. Anti-scatter grids and imaging system

We used two grids with grid ratios of 6:1 (G6) and 10:1 (G10), manufactured by Mitaya Co. (Tokyo, Japan). Both have a grid density of 40 lines/cm, an aluminum inter-spacer, and a focal distance of 1250 mm. The DR detector used was the AeroDR (Konica Minolta Co., Tokyo, Japan) indirect conversion flat panel detector (FPD), coupled to a caesium iodide (CsI) scintillator, with a 0.175 mm pixel pitch. The x-ray system used was RADspeed Pro, (Shimadzu Co., Kyoto, Japan) consisting of an inverter-type generator and a tube with a total filtration of 2.8 mm of aluminium (Al). Raw images, following gain correction were used for all measurements. The linearity of the raw images was verified by comparing free-in-air dose measured using a calibrated ionization chamber (Model 9015, 10X5-6 ionization chamber, Radcal, Monrovia, CA) and pixel values.

2.2. SIF measurement

SIF is estimated with

$$SIF = T_p\sqrt{B} \quad (1)$$

where T_P and B denote primary X-ray transmission and Bucky factor, respectively **[7,8,10-12]**, and the Bucky factor can be calculated by

$$B = \frac{P+S}{P_g+S_g} \quad (2)$$

where P and P_g are primary X-ray intensities without and with the grid, respectively, and S and S_g are scattered X-ray intensities. The scatter fraction (SF) is defined as

$$SF = \frac{S}{S+P} \quad (3)$$

Thus, SIF can be expressed as

$$SIF = \frac{P_g(P+S)}{P(P_g+S_g)\sqrt{B}} = \frac{1-SF_g}{1-SF} \cdot \frac{1}{\sqrt{B}} \quad (4)$$

using SF and SF_g without and with the grid, respectively. SF is typically measured by means of the beam stop method, and B can be calculated based on background signal levels in the image data for the beam stop method (SF measurement) with and without grid.

Fig. 1a shows the acquisition geometry for SF measurement. Acrylic (polymethylmethacrylate: PMMA) slabs with 300 × 300 mm^2 (900 cm^2) and 50 and 20 mm thicknesses were used to construct phantoms with 50, 70, 100, 150, and 200 mm thicknesses. The beam stop array device was composed of 5 × 5 Pb cylinders spaced 25 mm apart; each 6 mm in thickness and 3 mm in diameter were placed on the PMMA phantom **[13-17]**. Mean pixel values were measured within the region of interest (ROI) with a 10 pixel diameter positioned over each beam stop and ROIs on either side of the beam stop. The SF was then calculated from the ratio of ROI value within each beam stop to the average ROI value of the background, and the 25 SIF values were averaged. SF was measured at each thickness for different tube voltages of 60, 70, 80, 90, and 100 kV. The graduated lead beam stop method using different sizes of lead disk was not used because the 3 mm-diameter disk reported by Floyd et al. was used instead of the method within a 3% error **[13]**. The Bucky factor B was obtained by calculating a ratio of the

background ROI values with and without each grid. The exposure condition (mAs) for each thickness was determined by exposing the phantom without the grid and beam stop array, turning on the automatic exposure control system with a normal setting used clinically. The free-in-air dose was measured using the same ionization chamber described in Section 2.1, located at a 1200 mm distance from the X-ray focal spot. Then, the dose value was corrected to one corresponding at the phantom surface based on the inverse square law. **Table 1** shows the measured entrance surface air kerma (ESAK) values for respective conditions without backscatter, which were used in the experiments irrespective of the grid used.

For the 70 and 100 mm thickness, 150×150 mm^2 (225 cm^2), 200×200 mm^2 (400 cm^2), and 250×250 mm^2 (625 cm^2) field sizes were examined to investigate the SIF corresponding to field sizes of pediatric abdomen. Tube voltages were limited to 60, 70, and 80 kV.

2.3. Signal difference-to-noise ratio (*SDNR*)

Since an object contrast is no longer the dominant factor for image quality in DR, SDNR is a more relevant measure of the image quality, which is effective for cases with

different contrasts depending on radiation qualities and SFs **[18-20]**. As mentioned earlier, SIF is a useful method to evaluate the effectiveness of grid for different thicknesses; however, it cannot be used to evaluate the optimum tube voltage because SIF is a relative value and any contrast objects are not imaged in the SIF measurement. SDNR is calculated using signal intensities of signal S_O and background S_B and the standard deviation (SD) of the background as

$$SDNR = \frac{|S_O - S_B|}{SD_B} \quad (5)$$

Fig. 1b shows the acquisition geometry for bone and soft tissue contrasts and SDNR measurement. A PMMA plate and a plate made of a bone equivalent material (4120-220 BE-H-10, Kyoto Kagaku, Kyoto, Japan) both with a 10 mm thickness and 2 × 2 cm^2 area were placed on the phantom with each thickness. The PMMA plate was used to evaluate SDNR for soft-tissue. Mean pixel values were measured within ROIs with 55 × 55 pixels (approximately 100 mm^2), located on objects and backgrounds between the two objects. The background SD was also obtained from the background ROI. To essentially evaluate the tube voltage dependency of SDNR, a figure of merit (FOM) was calculated and expressed as

$$FOM = \frac{SDNR^2}{ESAK} \quad (6)$$

which is independent of the ESAK difference among the phantom thickness (see Table 1).

Table 1. Entrance surface air kerma (ESAK) obtained using a clinical setting of automatic exposure control system for each combination of PMMA thickness and tube voltage.

kV	PMMA Thickness (mm)				
	50	70	100	150	200
60	0.27	0.34	0.64	1.62	4.06
70	0.30	0.39	0.64	1.57	4.00
80	0.27	0.41	0.68	1.48	3.35
90	0.29	0.38	0.70	1.50	3.37
100	0.28	0.38	0.69	1.47	3.26

(mGy)

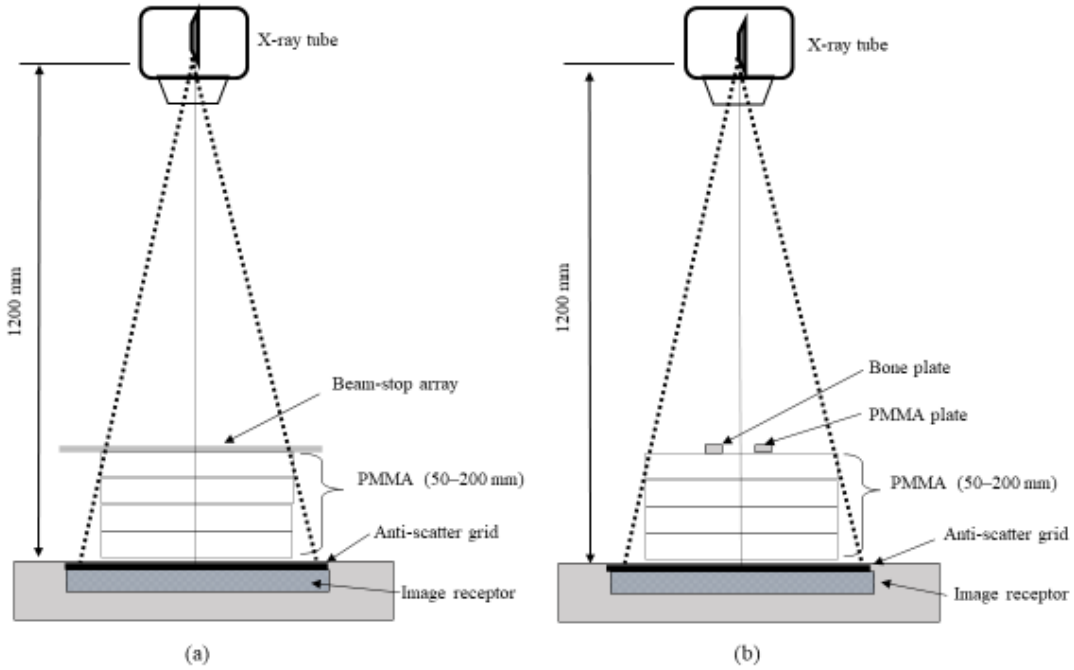

Fig. 1. Schematics of acquiring geometries for measurements of (a) scatter fraction (SF) and (b) signal-difference-to-noise ratio (SDNR).

Chapter 3

Results

3.1. Scatter fraction

Table 2 shows measured SFs. SF without grid (G–) ranged from 0.444 (50 mm thickness, 60 kV) to 0.841 (200 mm thickness, 100 kV). With G6, SF ranged from 0.163 (50 mm thickness, 60 kV) to 0.628 (200 mm thickness, 100 kV), and SF with G10 ranged from 0.118 (50 mm thickness, 60 kV) to 0.501 (200 mm thickness, 100 kV). The difference among tube voltages without the grid was negligible for all thicknesses, indicating variations from the average of <5% (from 2.5% for 200 mm thickness to 5.0% for 50 mm thickness). In contrast, SF with grid increased with elevated tube voltage. SF improvements by G6/G10 ranged from 25%/40% for the 200 mm thickness at 100 kV to 63%/74% for the 50 mm thickness at 60 kV. SFs in the field sizes of 225 cm^2, 400 cm^2, and 625 cm^2 are decreased by approximately 13%, 6%, and 3% for the 70 mm thickness and 14%, 6%, and 2% for the 100 mm thickness, respectively, compared with corresponding values of 900 cm^2.

Table 2. Scatter fraction (SF) results with and without grids with grid ratios of 6:1 (G6) and 10:1 (G10).

PMMA thickness (mm)	kV	G–	G6	G10
50	60	0.444	0.163	0.118
	70	0.451	0.180	0.129
	80	0.457	0.200	0.143
	90	0.460	0.219	0.161
	100	0.466	0.235	0.172
70	60	0.542	0.210	0.147
	70	0.546	0.235	0.163
	80	0.553	0.260	0.181
	90	0.561	0.283	0.202
	100	0.567	0.304	0.221
100	60	0.644	0.283	0.192
	70	0.653	0.311	0.213
	80	0.662	0.344	0.242
	90	0.664	0.373	0.266
	100	0.670	0.398	0.289
150	60	0.750	0.393	0.272
	70	0.756	0.431	0.304
	80	0.766	0.472	0.338
	90	0.773	0.502	0.374
	100	0.778	0.526	0.401
200	60	0.820	0.494	0.354
	70	0.826	0.533	0.390
	80	0.832	0.570	0.431
	90	0.836	0.603	0.468
	100	0.841	0.628	0.501

3.2. SNR improvement factor

Table 3 shows measured bone and soft tissue contrasts. As the tube voltage increases, the contrast of both substances decreases. Contrast ratios of 100 kV to 60 kV were more decreased with thicker thicknesses. For example, the contrast ratio of 0.734 for 5-cm PMMA with G10 decreased to 0.605 for 20-cm PMMA with G10.

Fig. 2a and **2b** show SIF variations as a function of the phantom thickness for G6 and G10, respectively. SIF increased with thickness at all tube voltages, and SIF of G10 was mostly superior to that of G6, except for 50mm thickness at all tube voltages and 70 mm thickness at 60 kV. With the minimum 50 mm thickness, all SIF values were <1.0; the worst value was 0.92 for G10 at 60 kV. SIFs exceeding 1.0 were given with ≥70 mm thicknesses, except for G10 at 60 kV that is not practical in clinical use due to its low dose efficiency (high Bucky factor). **Fig. 3a and 3b** show SIF variations as a function of the field size for 70 and 100 mm thicknesses, respectively. For the 70 mm thickness with field sizes of 400 cm^2, SIFs exceeding 1.0 were given only for G10 at 80 kV, whereas most conditions with the field size of 625 cm^2 presented SIFs exceeding 1.0, except for G10 at 60 kV. Thus, the grid use for the 70 mm thickness was not more advantageous with these smaller field sizes. For the 100 mm thicknesses, G6 and G10 at 70 kV and 80

kV indicated SIFs more than 1.07 with the 400 cm^2 field size and more than 1.10 with the 600 cm^2 field size.

Table 3 The result of signal intensities by PMMA phantom and bone phantom

PMMA (cm)	kV	Bone			PMMA		
		G-	G6	G10	G-	G6	G10
5	60	0.396	0.596	0.628	0.148	0.222	0.234
	70	0.364	0.543	0.577	0.140	0.209	0.222
	80	0.337	0.496	0.531	0.133	0.196	0.210
	90	0.316	0.458	0.491	0.128	0.186	0.200
	100	0.297	0.426	0.461	0.124	0.177	0.192
7	60	0.326	0.562	0.607	0.122	0.210	0.227
	70	0.301	0.506	0.554	0.115	0.194	0.213
	80	0.277	0.459	0.508	0.110	0.182	0.201
	90	0.257	0.420	0.467	0.104	0.171	0.190
	100	0.241	0.388	0.434	0.100	0.161	0.181
10	60	0.253	0.511	0.575	0.095	0.191	0.215
	70	0.230	0.456	0.521	0.088	0.175	0.200
	80	0.210	0.407	0.470	0.083	0.161	0.186
	90	0.197	0.367	0.430	0.080	0.149	0.175
	100	0.184	0.335	0.396	0.076	0.140	0.165
15	60	0.178	0.433	0.518	0.066	0.161	0.193
	70	0.161	0.377	0.461	0.062	0.145	0.177
	80	0.145	0.327	0.410	0.058	0.130	0.162
	90	0.133	0.291	0.366	0.054	0.118	0.149
	100	0.124	0.264	0.334	0.051	0.110	0.139
20	60	0.128	0.360	0.460	0.048	0.134	0.172
	70	0.115	0.309	0.404	0.044	0.119	0.155
	80	0.104	0.267	0.353	0.041	0.106	0.140
	90	0.096	0.232	0.311	0.039	0.094	0.127
	100	0.089	0.207	0.278	0.037	0.086	0.116

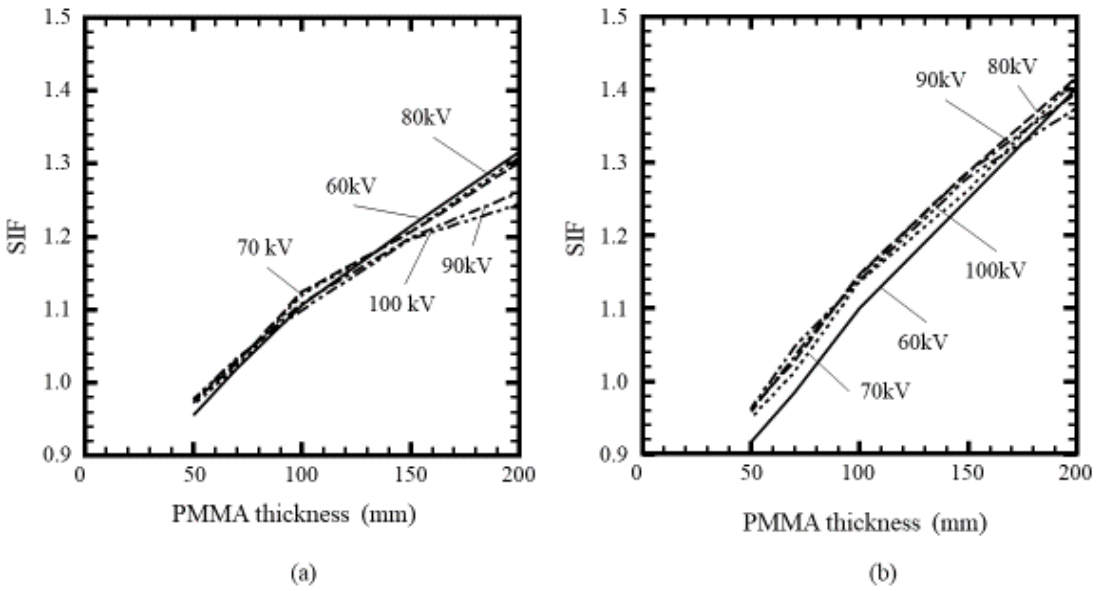

Fig. 2. SIF variations as a function of PMMA thickness using (a) G6 and (b) G10.

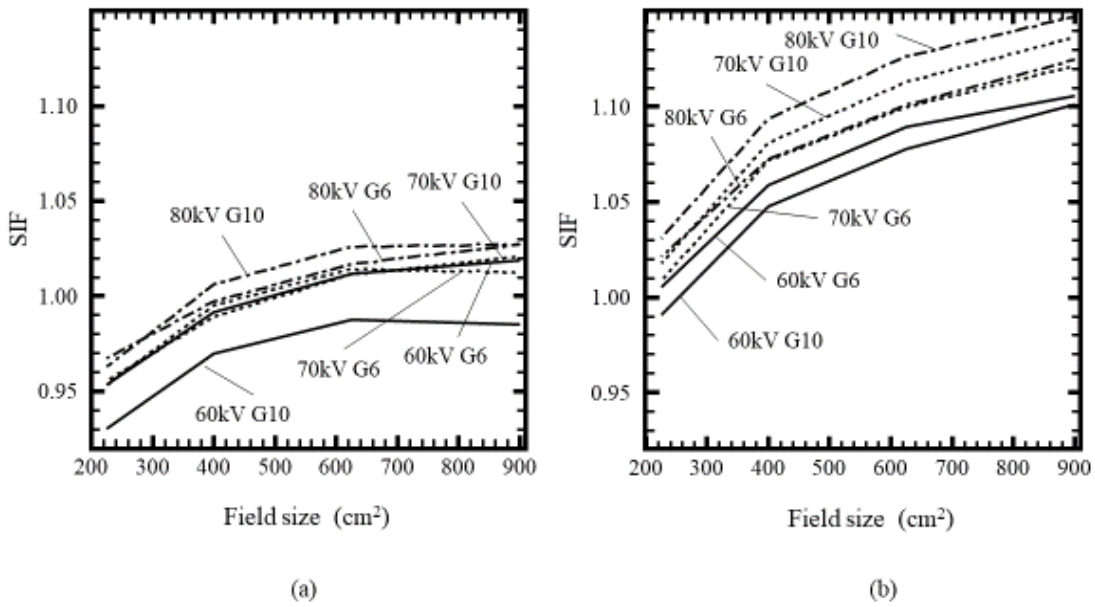

Fig. 3. SIF variations as a function of field size for (a) 70-mm and (b) 100-mm thicknesses.

3.3. Tube voltage dependency of FOM

Fig. 4 and 5 represent tube voltage dependencies of FOM for the bone and PMMA contrasts, respectively. With the bone contrast, the 50 mm thickness presented a weak tube voltage dependency where FOM decreased as the tube voltage increased. The 70–200 mm thicknesses indicated almost no tube voltage dependencies, but a little lower FOM at 60 kV with the 150 and 200 mm thicknesses was indicated. With the PMMA contrast, G6 with 50 and 70 mm thicknesses exhibited almost no dependencies, and for other conditions, FOM tended to increase from 60 kV to 80 kV and then to be almost constant.

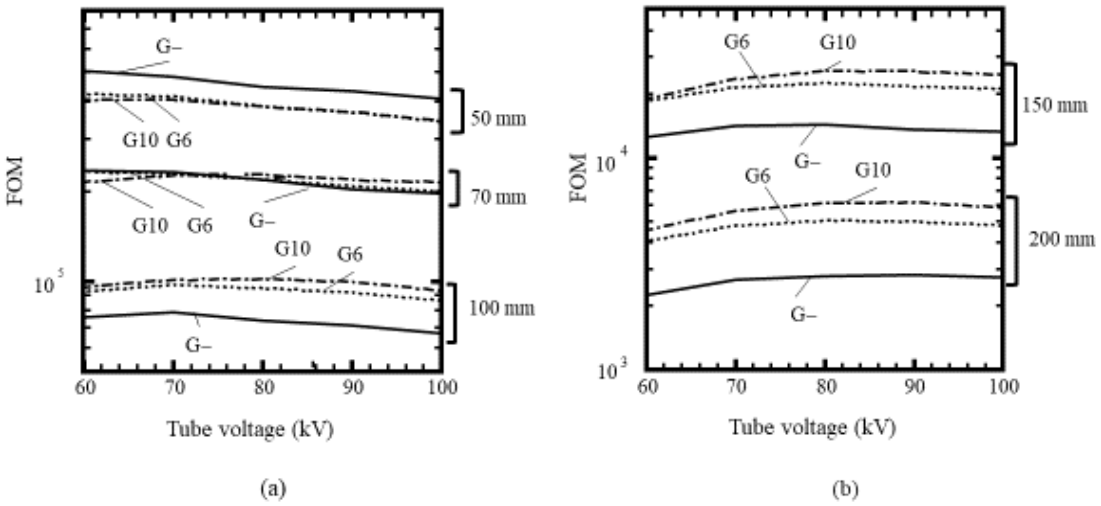

Fig. 4. Results of tube voltage dependencies in figure of merit (FOM) calculated as $SDNR^2/ESAK$ (SDNR: signal-difference-to-noise ratio, ESAK: entrance surface air kerma), for the bone contrast with (a) 50-, 70-, 100-mm thicknesses, and (b) 150- and 200-mm thicknesses.

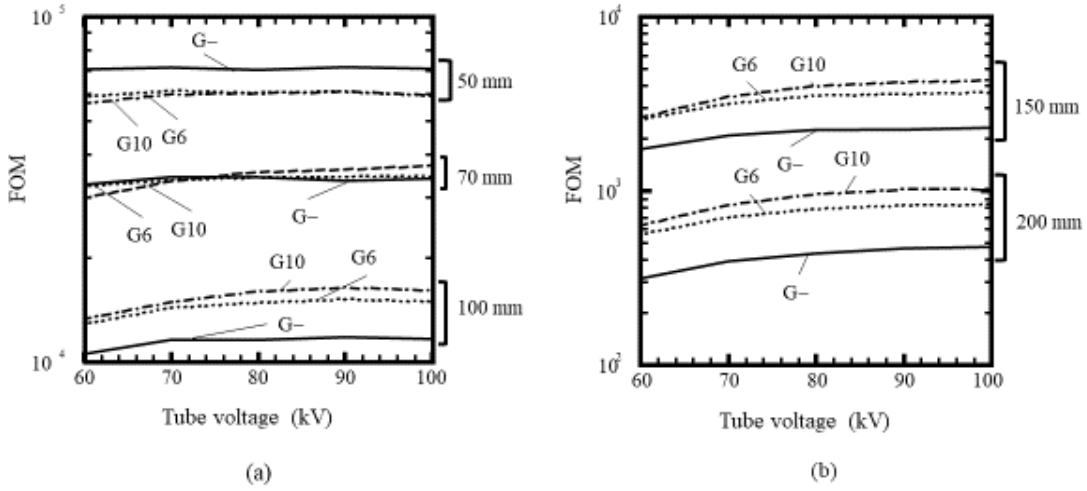

Fig. 5. Results of tube voltage dependencies in the FOM for the PMMA contrast with (a) 50-, 70-, 100-mm thicknesses, and (b) 150- and 200-mm thicknesses.

Chapter 4

Discussion

This study evaluated SIF variations as a function of thickness for different tube voltages and tube voltage dependencies of SDNR with and without grid. SIFs for smaller field sizes corresponding to infants and subjects with low thicknesses were also evaluated.

In addition to the results of previous studies using SIF, our investigation revealed detailed SIF properties for thicknesses of 50–100 mm that are around a threshold thickness of the selection of grid use. Furthermore, the tube voltage dependency of SDNR for 60–100 kV was analyzed to determine the best tube voltage for bone and soft tissues in the grid use. Since the G10 use for 70 mm thickness at 60 kV is not clinically realistic, our results demonstrated that SIF exceeded 1.0 with ≥70 mm thickness for the 900 cm^2 field size. For the smaller field sizes (225, 400, and 625 cm^2), the 70 mm thickness could mostly not exceed 1.0 with 225 cm^2 and 400 cm^2, and most SIFs with the 100 mm thickness exceeded 1.0. The SDNR investigation revealed that there is no notable tube voltage dependency for grid use.

Two American guidelines **[21, 22]** indicated that grids should be used sparingly in

pediatrics and should not be routinely used for extremity imaging or body parts with ≤100–120 mm thicknesses. Also, a European guideline indicated that grid is often unnecessary for infants and younger children and does not mention the thickness threshold for the grid use **[23]**. According to a study on patient size measured on computed tomography images **[24]**, the abdominal anteroposterior dimension for 1-year-olds is approximately 110 mm. In addition, a typical radiography field size in a previous report is approximately 400 cm^2 for 1-year-olds **[3]**. The field sizes of body parts with thicknesses around 100 mm, such as extremities and shoulder, approximately correspond to the field sizes of 400 and 625 cm^2 we used because their typical cassette sizes are 18 × 24 cm^2 and 24 × 30 cm^2. Therefore, we considered that 70 and 100 mm thicknesses should be evaluated, focusing on the field sizes of 400 cm^2 for infants and 400 and 600 cm^2 for the extremities and shoulder.

To select grids for infants, a dose reduction capability with grid can be accounted because the radiation dose can be reduced when the SIF of grid exceeds 1.0. Thus, we estimated the dose reduction capability R_G that can be calculated as $(1–1/SIF^2) \times 100\%$. For the 70 mm thickness, SIF values were <1.03 as shown in **Fig. 3a**; thus, the grid effectiveness is limited and R_G is <6%. In contrast, the grid use for 100 mm thickness is advantageous because SIFs of G10 at 70 kV and 80 kV with 400 cm^2 field size were 1.08

and 1.09, respectively, and R_{GS} are 14% and 16 %. With G6 at 70 kV and 80 kV, SIF was 1.07; thus, approximately 13% dose reduction is achieved. The PMMA (soft-tissue) contrasts with G6 and G10 at 70 kV measured for the SDNR evaluation was 43% and 54% higher than that of G– at 60 kV, respectively, while even at 80 kV, corresponding values were 29% and 40%, respectively. Thus, grids may contribute to not only dose reduction but also object contrast improvements that facilitate digital image processing. When the grid is used at the same dose of G–, the image quality (SNR) would be improved according to the SIF value.

For the 100 mm thickness with 625 cm^2 field size assuming conditions of extremities and shoulder, the SIFs at 70 kV and 80 kV ranged from 1.10 to 1.25. The bone contrast with G6 and G10 at 70 kV (80 kV) were 49 % and 61 % (34 % and 46 %) higher than that of G– at 60 kV, respectively. Thus, by using grids for the extremities and shoulder, image quality and object contrast are improved.

The tube voltage dependency of FOM with grid was not prominent for conditions corresponding to clinical use. G10 use at 60 kV for 50 and 70 mm thicknesses and 60 kV use for 150 and 200 mm thicknesses are not empirically practical, and thus these conditions should be excluded in the consideration. One indication in the results was that FOM at 60 kV for the 100 mm thickness was smaller compared to that for other tube

voltages, with the PMMA (soft-tissue) contrast, suggesting that 70 and 80 kV are recommend for 100-mm thicknesses. These results support a statement in a review paper that recommends the use grids at ≥70 kV **[4]**. Although FOMs of 90 kV and 100 kV were almost similar to those of 70 kV and 80 kV, such high tube voltages are not clinically applicable because the image contrast regularization in digital image processing may not properly work for low object contrasts due to high tube voltages.

This study has the following limitations. Although SIF is an established index, clinical studies used to validate our results are necessary. The phantoms used were constructed with acrylic slabs and had flat surfaces and a uniform content, and thus phantom thicknesses do not necessarily correspond to human body thicknesses. In addition, we did not investigate recent fiber grids because our purpose was to test the generally used grids with aluminum inter-spacers and covers, which are still prevalent in many hospitals. SIFs of grids with fiber inter-spacers were reported to provide SIFs higher than our results **[8]**, and thus the grid used for 100 mm thickness may become definitely effective with 400 cm^2 field size corresponding to those of 1-year-old infants.

Chapter 5

Conclusion

We have investigated the appropriate object thickness to start using anti-scatter grids (grids), using two generally used grids with grid ratios of 6 and 10 (G6 and G10) for different 50–200 mm thicknesses at tube voltages of 60–100 kV.

Our results showed that using G6 and G10 with aluminum inter-spacers and aluminum covers, SIF exceeded 1.0 for ≥70 mm thickness with the 900 cm^2 field size. SIFs of G10 at 70 kV and 80 kV were 1.08 and 1.09 with a small field size of 400 cm^2 corresponding to abdomen of 1-year-old infants, for which the estimated dose reduction capabilities were approximately 15%. The 100 mm thickness with 625 cm^2 field size corresponding to examinations using a cassette size of 18 × 24 cm^2 showed 10% to 25% SNR improvements. The tube voltage dependency of image quality evaluated with SDNR for the grid use was not notable for tube voltages from 70 to 100 kV. Thus, our results indicated that the grid-use for the 100 mm thickness, which has been excluded from conditions recommendable of grid use, may reduce the radiation dose or improve the image quality at the same dose for gridless.

Declarations

This research did not receive any specific grant from funding agencies in the public, commercial, or not-for-profit sectors.

References

[1] Don S, Macdougall R, Strauss K, Moore QT, Goske MJ, Herrmann T, et al. Image gently campaign back to basics initiative: Ten steps to help manage radiation dose in pediatric digital radiography. Am J Roentgenol 2013;200:431–6. doi:10.2214/AJR.12.9895.

[2] Knight SP. A paediatric X-ray exposure chart. J Med Radiat Sci 2014;61:191–201. doi:10.1002/jmrs.56.

[3] Fritz S, Jones AK. Guidelines for anti-scatter grid use in pediatric digital radiography. Pediatr Radiol 2014;44:313–21. doi:10.1007/s00247-013-2824-9.

[4] Herrmann TL, Fauber TL, Gill J, Hoffman C, Orth DK, Peterson PA, et al. Best practices in digital radiography. Radiol Technol 2012; 84 :83 – 9.

[5] Dick CE, Soares CG, Motz JW. X-ray scatter data for diagnostic radiology. Phys Med Biol 1978;23:003. doi:10.1088/0031-9155/23/6/003.

[6] Kalender W. Monte Carlo calculations of X-ray scatter data for diagnostic radiology. Phys Med Biol 1981;26:835–49. doi:10.1088/0031-9155/26/5/003.

[7] Chan HP, Lam KL, Wu YZ. Studies of performance of antiscatter grids in digital radiography: effect on signal-to-noise ratio. Med Phys 1990;17:655–64.

doi:10.1118/1.596496.

[8] Fetterly KA, Schueler BA. Experimental evaluation of fiber-interspaced antiscatter grids for large patient imaging with digital x-ray systems. Phys Med Biol 2007;52:4863–80. doi:10.1088/0031-9155/52/16/010.

[9] Sandborg M, Dance DR, Carlsson GA, Persliden J. Selection of anti-scatter grids for different imaging tasks: The advantage of low atomic number cover and interspace materials. Br J Radiol 1993;66:1151–63. doi:10.1259/0007-1285-66-792-1151.

[10] Moore CS, Wood TJ, Saunderson JR, Beavis AW. Correlation between the signal-to-noise ratio improvement factor (K SNR) and clinical image quality for chest imaging with a computed radiography system. Phys Med Biol 2015;60:9047–58. doi:10.1088/0031-9155/60/23/9047.

[11] Mizuta M, Sanada S, Akazawa H, Kasai T, Abe S, Ikeno Y, et al. Comparison of anti-scatter grids for digital imaging with use of a direct-conversion flat-panel detector. Radiol Phys Technol 2012;5:46–52. doi:10.1007/s12194-011-0134-1.

[12] Cunha DM, Tomal A, Poletti ME. Evaluation of scatter-to-primary ratio, grid performance and normalized average glandular dose in mammography by Monte Carlo simulation including interference and energy broadening effects. Phys Med Biol 2010;55:4335–59. doi:10.1088/0031-9155/55/15/010.

[13] Floyd CE, Lo JY, Chotas HG, Ravin CE. Quantitative scatter measurement in digital radiography using a photostimulable phosphor imaging system. Med Phys 1991;18:408–13. doi:10.1118/1.596687.

[14] Samei E, Lo JY, Yoshizumi TT, Jesneck JL, Dobbins JT, Floyd CE, et al. Comparative scatter and dose performance of slot-scan and full-field digital chest radiography systems. Radiology 2005;235:940–9. doi:10.1148/radiol.2353040516.

[15] Samei E, Ranger NT, MacKenzie A, Honey ID, Dobbins JT, Ravin CE. Effective DQE (eDQE) and speed of digital radiographic systems: An experimental methodology. Med Phys 2009;36:3806–17. doi:10.1118/1.3171690.

[16] Ranger NT, Mackenzie A, Honey ID, Dobbins III JT, Ravin CE, Samei E. Extension of DQE to include scatter, grid, magnification, and focal spot blur: a new experimental technique and metric. Proc SPIE 2009;7258:72581A-72581A – 12. doi:10.1117/12.813779.

[17] Samei E, Ranger NT, Dobbins JT, Ravin CE. Effective dose efficiency: an application-specific metric of quality and dose for digital radiography. Phys Med Biol 2011;56:5099–118. doi:10.1088/0031-9155/56/16/002.

[18] Samei E, Dobbins JT, Lo JY, Tornai MP. A framework for optimising the radiographic technique in digital X-ray imaging. Radiat Prot Dosimetry 2005;114:220–9. doi:10.1093/rpd/nch562.

[19] Åslund M, Cederström B, Lundqvist M, Danielsson M. Scatter rejection in multislit digital mammography. Med Phys 2006;33:933. doi:10.1118/1.2179122.

[20] Kawashima H, Ichikawa K, Nagasou D, Hattori M. X-ray dose reduction using additional copper filtration for abdominal digital radiography: Evaluation using signal difference-to-noise ratio. Phys Med. 2017;34(2):65-71. doi.org/10.1016/j.ejmp.2017.01.015

[21] American College of Radiology. ACR-SPR practice guideline for general radiography, Reston, VA: American College of Radiology, 2017 www.acr.org/-/media/ACR/Files/Practice-Parameters/Rad-Digital.pdf. Accessed May 10, 2019

[22] American College of Radiology. ACR-SPR practice guideline for general radiography, Reston, VA: American College of Radiology, 2018 www.acr.org/-/media/ACR/Files/Practice-Parameters/RadGen.pdf. Accessed May 10, 2019

[21] Andriole KP, Ruckdeschel TG, Flynn MJ, Hangiandreou NJ, Jones AK, Krupinski E, et al. ACR–AAPM–SIIM Practice Guideline for Digital Radiography. J Digit Imaging 2013;26:26–37. doi:10.1007/s10278-012-9523-1.

[22] American College of Radiology. ACR-SPR practice parameter for general radiography, Reston, VA: American College of Radiology, 2018 www.acr.org/-/media/ACR/Files/Practice-Parameters/RadGen.pdf. Accessed May 10, 2019

[23] European Commission. European Guidelines on Quality Criteria for Diagnostic Radiographic Images in Paediatrics. Publication EUR 16261 EN. Brussels, Belgium: European Commission; 1996.

[24] Kleinman PL, Strauss KJ, Zurakowski D, Buckley KS, Taylor GA. Patient size measured on CT images as a function of age at a tertiary care children's hospital. Am J Roentgenol 2010;194:1611–9. doi:10.2214/AJR.09.3771.

Biography

1. Kunitomo H, Ichikawa K. Signal-to-noise ratio improvements using anti-scatter grids with different object thicknesses and tube voltages. Phys Med. 2020;73:105-110. doi:10.1016/j.ejmp.2020.04.014
2. Kan H, Uchida Y, Arai N, Ueki Y, Aoki T, Kasai H, Kunitomo H, Hirose Y, Matsukawa N, Shibamoto Y. Simultaneous voxel-based magnetic susceptibility and morphometry analysis using magnetization-prepared spoiled turbo multiple gradient echo. NMR Biomed. 2020;33(5):e4272. doi:10.1002/nbm.4272
3. Arai N, Kan H, Ogawa M, Uchida Y, Takizawa M, Omori K, Miyati T, Kasai H, Kunitomo H, Shibamoto Y. Visualization of Nigrosome 1 from the Viewpoint of Anatomic Structure. AJNR Am J Neuroradiol. 2020;41(1):86-91. doi: 10.3174/ajnr.A6338
4. Kan H, Eguchi Y, Tsuchiya T, Kondo T, Kitagawa Y, Mekata Y, Fukuma H, Yoshida R, Kasai H, Kunitomo H, Hirose Y, Shibamoto Y. Geometric discrepancy of image-guided radiation therapy in patients with prostate cancer without implanted fiducial markers using a commercial pseudo-CT generation method. Phys Med Biol. 2019;64(6):06NT01. Published 2019 Mar 8. doi:10.1088/1361-6560/ab02cc
5. Kan H, Arai N, Takizawa M, Kasai H, Kunitomo H, Hirose Y, Shibamoto Y.

Improvement of Signal Inhomogeneity Induced by Radio-frequency Transmit-related Phase Error for Single-step Quantitative Susceptibility Mapping Reconstruction. Magn Reson Med Sci. 2019;18(4):276-285. doi: 10.2463/mrms.tn.2018-0066

6. Kan H, Arai N, Takizawa M, Omori K, Kasai H, Kunitomo H, Hirose Y, Shibamoto Y. Background field removal technique based on non-regularized variable kernels sophisticated harmonic artifact reduction for phase data for quantitative susceptibility mapping. Magn Reson Imaging. 2018;52:94-101. doi: 10.1016/j.mri.2018.06.006
7. Kan H, Kasai H, Arai N, Kunitomo H, Hirose Y, Shibamoto Y. Background field removal technique using regularization enabled sophisticated harmonic artifact reduction for phase data with varying kernel sizes. Magn Reson Imaging. 2016;34(7):1026-1033. doi: 10.1016/j.mri.2016.04.019
8. Kan H, Arai N, Kasai H, Kunitomo H, Hirose Y, Shibamoto Y.Quantitative susceptibility mapping using principles of echo shifting with a train of observations sequence on 1.5T MRI. Magn Reson Imaging. 2017;42:37-42. doi: 10.1016/j.mri.2017.05.002
9. Higashide R, Ichikawa K, Kunitomo H, Ohashi K. Application of a variable filter for presampled modulation transfer function analysis with the edge method. Radiol Phys

Technol. 2015;8(2):320-330. doi: 10.1007/s12194-015-0325-2

10. Ohashi K, Ichikawa K, Hara M, Kawai T, Kunitomo H, Higashide R, Shibamoto Y. Examination of the optimal temporal resolution required for computed tomography coronary angiography. Radiol Phys Technol. 2013 Jul;6(2):453-60. doi: 10.1007/s12194-013-0218-1.

11. 國友 博史, 小山 修司, 東出 了, 市川 勝弘, 服部 真澄, 岡田 陽子, 林 則夫, 澤田 道人．DR システムにおける DQE 測定時の各因子の測定精度に関する検討．日本放射線技術学会雑誌．2014；7（7）： 653-661．doi: 10.6009/jjrt.2014_JSRT_70.7.653

12. 國友 博史, 市川 勝弘, 東出 了, 大橋 一也．低線量領域における Digital Radiography の物理的画質特性の検討．日本放射線技術學會雑誌．2012；68（8）: 961-969．doi:10.6009/jjrt.2012_JSRT_68.8.961

13. 大橋 一也, 市川 勝弘, 東出 了, 國友 博史． コンピュータ制御による冠動脈 CT 対応動態評価用ファントムを用いた EMR と DSCT との比較検討．日本放射線技術學會雑誌．2011；67(8), 880-887．doi：10.6009/jjrt.67.880

14. 國友 博史, 市川 勝弘, 東出 了, 大橋 一也． 澤田 道人, ディジタルノイズパワースペクトルの解析時の誤差要因の検討．日本放射線技術學會雑誌．2010；66(7), 734-742．doi：10.6009/jjrt.66.734

15. 東出 了, 市川 勝弘, 國友 博史, 大橋 一也, 川野 誠. 角度計測誤差が presampled MTF へ及ぼす影響の検証と角度計測の最適手法の提案. 日本放射線技術學會雑誌 . 2009 ; 65(2), 245-253. doi : 10.6009/jjrt.65.245

16. 東出 了, 市川 勝弘, 國友 博史, 澤田 道人. エッジ法による presampled MTF の簡便な解析方法の提案と検証. 日本放射線技術學會雑誌 2008 ; 64(4), 417-425. doi : 10.6009/jjrt.64.417

17. 市川 勝弘, 國友 博史, 櫻井 貴裕, 大橋 一成, 杉山 雅之, 宮地 利明, 宮地 利明, 藤田 広志. 矩形波チャート像のフーリエ変換によるプリサンプリング MTF の新しい測定法. 日本放射線技術学会雑誌. 2002 ; 58(9), 1261-1267. doi : 10.6009/jjrt.KJ00001364806

18. 笠井 治昌, 田中 武志, 春藤 英雄, 今澤 正好, 間瀬 光人, 宮地 利明, 伴野 辰雄, 大橋 一也, 櫻井 貴裕, 國友 博史, 市川 勝弘, 樋口 真, 磯山 茂. phase-contrast cine MRI による頭蓋内脳脊髄液循環動態の解析. 日本放射線技術学会雑誌 1997 ; 53(7), 791-797. doi : 10.6009/jjrt.KJ00001355820